

An Analysis of DES Cluster Simulations through the IMCAT and Shapelets Weak Lensing Pipelines

M.S.S. Gill^{1,4*}, J.C. Young¹, J.P. Draskovic¹, K. Honscheid¹, H. Lin²,
N. Kuropatkin², P. Martini^{1,3}, E. Rozo^{1,5}, G.N. Smith¹, D.H. Weinberg^{1,3}

¹ *Center for Cosmology and AstroParticle Physics, The Ohio State University, Columbus, Ohio 43210, USA*

² *The Fermi National Accelerator Laboratory, Batavia, Illinois 60510, USA*

³ *Department of Astronomy, The Ohio State University, Columbus, Ohio 43210, USA*

⁴ *The Kavli Institute for Particle Astrophysics and Cosmology, Mail Stop 29, PO Box 20450, Stanford, California 94309, USA*

⁵ *Einstein Fellow, The Kavli Institute for Cosmology and Astro Physics, 5640 South Ellis Avenue, Chicago, Illinois 60637, USA*

25 May 2010

ABSTRACT

This is the first paper of a series in which we examine the ability of some current weak gravitational lensing pipelines to determine galaxy cluster masses from this technique. This first exercise is done on a fairly simple image, more realistic images will follow. Our main intent in this endeavor is to test shape measurement pipelines in the high shear regime on a cluster simulation which includes details such as a PSF which varies across the image. Because we focus on this issue initially, we chose optimal and thus somewhat unrealistic conditions, e.g. it is clearer in our simulated images than in real data where to make the star-galaxy separation cuts, there is no confusion of cluster members and background galaxies when we make color cuts, and we have perfect redshift information for all the galaxies. We have run two completely independent weak lensing analysis pipelines on this set simulated images of a massive galaxy cluster with a singular isothermal sphere profile (with a galaxy velocity dispersion $\sigma_v = 1250$ km/sec). The suite of images was constructed using the simulation tools developed by the Dark Energy Survey. We find that for this image with its limited realism, both weak lensing pipelines can accurately recover the input velocity dispersion. We also demonstrate how choices of some cuts influence the final shear profile and σ_v measurement. Analogously to the STEP program, we make all of these cluster simulation images publically available for other groups to analyze through their own weak lensing pipelines.

Key words: Cluster Weak Lensing – Stage III Photometric Surveys – Dark Energy Survey

1 INTRODUCTION

Gravitational weak lensing, by both galaxy clusters and large scale structure as cosmic shear, has become one of the most promising observational avenues in recent times to place constraints on cosmological parameters and models (e.g. Albrecht et al. 2006, Peacock et al. 2006, Abbott et al. 2005). This is partly because it does not suffer from the inherent uncertainties involved in extrapolating cluster masses from other measurement techniques such as galaxy population richness class, x-ray luminosity of the hot intracuster gas, or galaxy velocity dispersion. In some sense,

cluster weak lensing is the most direct measure of the total mass of a cluster, both seen and unseen. It is thus highly critical to ascertain exactly how accurate and precise the results from available current pipelines are in both the cluster and cosmic shear contexts. The cosmic shear context has especially been tested in recent years through the STEP and GREAT collaborations (Massey et al. 2007a, Heymans et al. 2005, Bridle et al. 2008, Bridle et al. 2010), but there has until now been no analogous collaborative effort to verify the validity of lensing pipelines in the high shear context of cluster weak lensing. With the public release of the images used in this analysis, we aim to begin rectifying this in anticipation of upcoming major Stage III and Stage IV surveys

* Email: msgill@astronomy.ohio-state.edu

(Albrecht et al. 2006), which will collect very large amounts of data useful for cluster weak lensing.

In the case of the STEP and GREAT programs, sets of simulated images were made with the aim especially of comparing and optimizing pipelines designed for the measurement of cosmic shear. For this purpose, having images with constant shear and constant Point Spread Function (PSF) across the field was sufficient for verifying several of the primary properties of the pipelines. However, for cluster weak lensing analyses we know that the shear will vary both in magnitude and direction across the field. Thus to test pipelines for applicability to cluster weak lensing analyses, it is more suitable and realistic to make simulated images which incorporate variation of both the shear and the PSF across the field. As a first step, we did this by making simulated images in which an isothermal sphere shear is applied across the entire focal plane, and which further incorporate a PSF that varies linearly in anisotropy size and magnitude across each CCD though in an identical pattern across each CCD.

Using the DETF terminology, one example of a major upcoming Stage III observational campaign is the Dark Energy Survey (DES) (Abbott et al. 2005), scheduled to begin taking data in the Fall of 2011. DES will use four main techniques to place constraints on Dark Energy: (1) galaxy cluster number count distributions, (2) weak lensing cosmic shear measurements, (3) galaxy angular clustering measurements, and (4) distance measurements to Type Ia supernovae. Cluster weak lensing to determine cluster masses, and other properties such as concentrations, is also one of the integral components of the DES program, and will play an important role in the calibration of the first technique in the above list.

As part of the preparation for DES, weak lensing pipelines are being thoroughly tested for accuracy on simulations before the survey begins. In addition, the DES data management pipeline and analysis tools are being extensively exercised in pre-observation DES Data Challenges with realistic images. Following from these, and using the tools developed for the Data Challenges, we constructed a set of images containing a simulated galaxy cluster. We then processed these images through two completely independent weak lensing pipelines to probe how well the shear measurements are able to reconstruct the cluster mass. We also studied how different configuration and selection choices in the weak lensing pipelines affect the final cluster mass reconstruction.

This was our first step in a series where we will be ultimately process multiple cluster images through the same pipelines in order to do statistical tests of how well we are able to reconstruct the input cluster halo masses. For this first test, to focus on the issue of how well the pipelines determine the object shapes, we chose optimal and therefore somewhat unrealistic conditions for our cluster: e.g. it is clearer in our simulation than in real data where to make the star-galaxy separation cuts, there is no confusion of cluster members and background galaxies when we make color cuts, and we have perfect redshift information on each galaxy. Nonetheless, a fairly realistic redshift and color distribution for galaxies is used, as well as a realistic stellar distribution from our own Galaxy (see Sec. 2.1).

We analyzed the sample cluster images with two

pipelines based on publically available weak lensing codes: IMCAT – an implementation of the Kaiser, Squires, & Broadhurst (Kaiser et al. 1995) method – and Shapelets (Refregier 2003), and we present the results in this paper. It will be very useful to test multiple weak lensing pipelines on these cluster simulations, and we have made them publically available to the wider cosmological and weak lensing communities for this purpose at the following website: [<http://ccapp.osu.edu/DEScluster>].

The structure of the paper is as follows: in Section 2 we describe the simulated cluster. In Section 3 we describe the overall pipeline flow, object extraction and processing as well as our tests for the PSF removal procedures on the simulated cluster. In Section 4 we give our results, in Section 5 we show how the results vary with certain cuts, and in Section 6 we give our conclusions.

2 SIMULATED CLUSTER IMAGE PROPERTIES

2.1 Description of Background Galaxy Properties

Several cluster images were created with the gravitational weak lensing shear determined by the Singular Isothermal Sphere (SIS) model using the tools developed by the DES simulation group. Objects in the simulated images came from the same simulated galaxy and stellar catalogs used to populate image simulations generated for the annual DES Data Challenge process, which is carried out to help develop and test DES data processing and science analysis pipelines. Specifically, the catalogs used in this paper were the ones employed for the so-called DES “Data Challenge 4,” carried out in 2008-2009.

The galaxy catalogs used the publically available Hubble Volume (Colberg et al. 2000) as the parent dark matter N-body simulation box. Specifically the Λ CDM Hubble Volume simulation was used, with cosmology $\Omega_M = 0.3, \Omega_\Lambda = 0.7, h = 0.7, \sigma_8 = 0.9$ and a light cone with redshift limit $z = 1.4$. Galaxies were assigned to Hubble Volume dark matter particles using the ADDGALS method (see Appendix A of Gerdes et al. 2009, Wechsler et al. 2009, Wechsler 2004), whereby each galaxy was assigned the properties of a real Sloan Digital Sky Survey (SDSS) galaxy, and the procedure reproduces the local luminosity-color-density correlations from the SDSS. ADDGALS also reproduces the magnitude-dependent 2-point function, which is important to get correct cluster color-magnitude diagrams. In particular, to populate the galaxies in the image we used the Data Challenge 4 DES mock galaxy catalog, which covers a 573 deg^2 subset of the Hubble Volume sky area. This galaxy catalog has a surface density of about 13 galaxies per arcmin^2 down to an apparent magnitude limit in the i band of about $i = 24$. The luminosity function model used was that of Blanton et al. (2003) for the SDSS, with simple passive luminosity evolution applied (M_* brightens by 1.3 mag per unit redshift) irrespective of galaxy type. No redshift evolution beyond the local SDSS color-environment correlations was included. Galaxies were assigned shape parameters using shapelet coefficients (Refregier 2003), where the master shapelet coefficient distribution used was derived from a set of about 18,000 galaxies i -band CFHT MegaCam images,

taken from the public Cosmic Evolution Survey (COSMOS; Scoville et al. (2007)) data set¹. The CFHT images were first PSF-corrected by fitting stars to Moffat profiles, using the GALFIT program Peng, C.Y., et al. (2002). These PSFs were then used in the shapelets decompositions, which were carried out to order $n=15$, corresponding to using a total of 136 shapelet coefficients to describe each galaxy. The COSMOS/CFHT galaxies were assigned to the DES mock catalog galaxies using a simple nearest neighbor matching in the space of $griz$ magnitudes. No size or shape evolution was included other than redshift effects due to cosmology.

The stellar catalogs were based on real USNO-B stars (Monet et al. 2003) at the bright end ($r < 20$) and simulated stars at the faint end ($r > 20$), with the latter derived from a web based tool employing the Besancon stellar population synthesis model for our Galaxy² to generate simulated stars.

2.2 Details of Cluster Simulation

The simulated cluster is located at a redshift of 0.33, with $M_{200} = 2.9 \cdot 10^{14} M_{\odot}$, $r_{200} = 1.3$ Mpc and $\sigma_v = 1250$ km/sec, where M_{200} (r_{200}) is the mass (radius) out to a distance within which the average overdensity is 200 times the critical density of the universe at that redshift and σ_v is the velocity dispersion for an SIS profile (see Sec. 4.1 and for details on SIS properties see e.g. Sec. 3.1 of Narayan & Bartelmann (1996)). In order to avoid the strong lensing regime within the Einstein radius, which for this cluster for sources at $z = 1$ is about $27''$ (see Sec. 4.1), the shear is set to zero for objects within a certain radius. To be conservative we choose the value of this radius by excluding the region where objects would have tangential shear $\gamma_t > 0.2$ in the limit of $z \rightarrow \infty$, which corresponds to the area within a radius of about $100''$ from the cluster center. Using the pixel scale of the Dark Energy Camera (DECam) of 0.27 arcseconds per pixel (Honscheid et al. 2008), this corresponds to being within about 400 pixels from the cluster center. Except for this region, galaxy objects have SIS shear assigned accordingly across the full 3 square degree image mosaic. To get some sense of the scale of the shear variation, for a source at $z = 1$ the shear falls to about $\gamma = 0.02$, at a radius of $20'$ (6 Mpc) from the cluster center, roughly one third of the image plane radius.

Each galaxy object generated according to this prescription has five magnitudes in the SDSS-like filters g, r, i, z and y , as well as an assigned redshift, which are all contained in truth catalog files. Seven image files were produced with varying levels of complexity, and their properties are summarized in Table 1. Partial images for five of the files are shown in Fig. 2. In order to test how the pipelines vary for differing noise levels, there are three levels of noise included in the simulated images: No Noise, LN (Low Noise) and HN (High Noise). The LN images are what would be seen by DES with a 600 s exposure with readout and object photon noise included but without sky noise. The effects of the sky noise are present in the HN images which have a 13 times higher noise level. Our HN images should be fairly similar

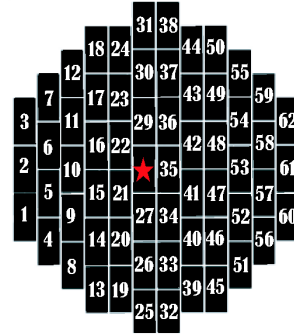


Figure 1. A graphical representation of the image plane with the standard DES CCD numbering. The red star marks the cluster center.

to nominal DES exposures which will be 100 seconds long with 5 passes throughout the survey.

2.3 Description of Simulated Images

The DES focal plane consists of 62 imaging CCDs, each with $x(y)$ dimensions of 2048 (4096) pixels. The image plane is shown in Fig. 1. Since the pixel scale of the DECam is 0.27 arcseconds per pixel, the radius of the image plane is ~ 65 arcminutes, and the field of view is ~ 3 square degrees.

The truth catalog contains many pieces of information about each object, the most useful for our purposes being:

- (RA, DEC) and (x, y) pixel positions,
- whether the object is a star or a galaxy,
- redshift,
- g, r, i, z, y magnitudes,
- SIS shear

For simplicity, the images were made only in the r -band³, but as noted above, the truth catalog contains the magnitudes for four other bands for each object, which are assigned according to the prescription described in Sec. 2.1, and we do not expect r and i -band galaxy shapes to be significantly different at the level of accuracy aimed for in this work. To apply the shear from the cluster, the exact SIS value for a given location in the image plane is convolved with the intrinsic object ellipticity through the Shapelets shear convolution algorithm (Refregier 2003). For simplicity, magnification from the cluster was *not* accounted for in the images.

To make the cluster simulation more realistic, five of the seven images incorporate a PSF that affects all the objects in the image. This PSF convolution is applied not using Shapelets but instead by using fast Fourier transforms, so that compute time is kept reasonable but the complexity of the PSFs can still be increased significantly later. This PSF varies in ellipticity and size across each CCD, but it has an identical form for all 62 CCDs. The PSF is modeled with two pieces: the first is an isotropic Gaussian-smearing

¹ The catalog for the step in the Data Challenges is being drawn from space-based images for superior resolution.

² <http://model.obs-besancon.fr/>

³ In part, this is because one of motivations at the very beginning of our study was to simulate images somewhat similar to real LBT cluster images in the r -band which we had in hand already

Table 1. Brief description of the simulated images.

File Description	Noise	Shear	Included Objects
Original Non-sheared	None	None	Background Galaxies
Sheared	None	Cluster Shear	Background Galaxies
High Noise	High	Cluster Shear	Background Galaxies
High Noise + PSF Applied	High	Cluster Shear + PSF	Background Galaxies Stars
High Noise + PSF Applied + Foreground Galaxies	High	Cluster Shear + PSF	Background Galaxies Stars Foreground Galaxies
Low Noise + PSF Applied	Low	Cluster Shear + PSF	Background Galaxies Stars
Low Noise + PSF Applied + Foreground Galaxies	Low	Cluster Shear + PSF	Background Galaxies Stars Foreground Galaxies

Table 2. Rounded initial numbers of objects in the labelled column categories of Table 1, all in thousands. No cut has been applied to the files with foreground galaxies, so all of these are included in the yield for Galaxy Objects. 100k galaxies across the DES focal plane would correspond to about 9 galaxies per square arcminute.

File	Raw Objects (thousands)	Cleaned Objects (thousands)	Stellar Objects (thousands)	Galaxy Objects (thousands)
Original	105	28	n/a	28
Sheared	105	28	n/a	28
High Noise	46	44	n/a	44
HN+PSF	59	52	11	26
HN+PSF+ Foreground	74	66	11	40
Low Noise+PSF	128	105	14	78
LN +PSF+ Foreground	146	115	14	89

function with a slowly linearly increasing width varying in 10 equally spaced steps, each of about 0.02 pixels. In total, the width varies from 2.9 pixels at the bottom to 3.1 pixels at the top of the CCD. The second piece of the PSF is an anisotropic component whose total ellipticity linearly decreases in the same 10 steps from the bottom to the top of each CCD. In total, this ellipticity varies from 0.6% at the bottom to 0.2% at the top of the CCD. While we use a fairly simplistic Gaussian PSF for this study, the next phase of our simulations will incorporate atmospheric refraction, optical misalignment effects, as well as an underlying instrumental DECam PSF model, all of which will introduce more realistic and interesting spatial PSF variations.

The PSF convolutions are done using fast Fourier transforms (FFTs). This was because we found that the relatively low order ($n = 6$) shapelets that we were using were not adequate to describe the DECam optical PSFs, and that going to significantly higher shapelets order was not computationally efficient, as the shapelets PSF convolution was a large fraction of the total compute time. Thus we switched to FFTs as the compute time could be kept reasonable and

the complexity of the PSFs could still be increased significantly.

Fig. 3a shows the average of the two components of ellipticities for the image-selected stars in linear strips in each CCD. The inclination of each line segments indicates the direction of the average ellipticity, and the length indicates its magnitude. It can be seen that the magnitude of the ellipticity becomes steadily smaller towards the top of the CCD. In Fig. 3b we plot the average of a linear function of the full width at half maximum (FWHM) for the image-selected stars in a grid on each CCD. Here, the radius of each circle indicates the scaled FWHM magnitude for that strip. It can be seen that towards the top of the CCD the FWHM becomes steadily larger.

We note here that in our simply repeated PSF, that though it is true that the effect of the ellipticity pattern is averaged out in annuli, for accurate σ_v extraction, it is critical that not only the PSF-imposed ellipticity pattern be removed from the objects, but that the effect of the circular smearing part of the PSF, which effectively reduces the sig-

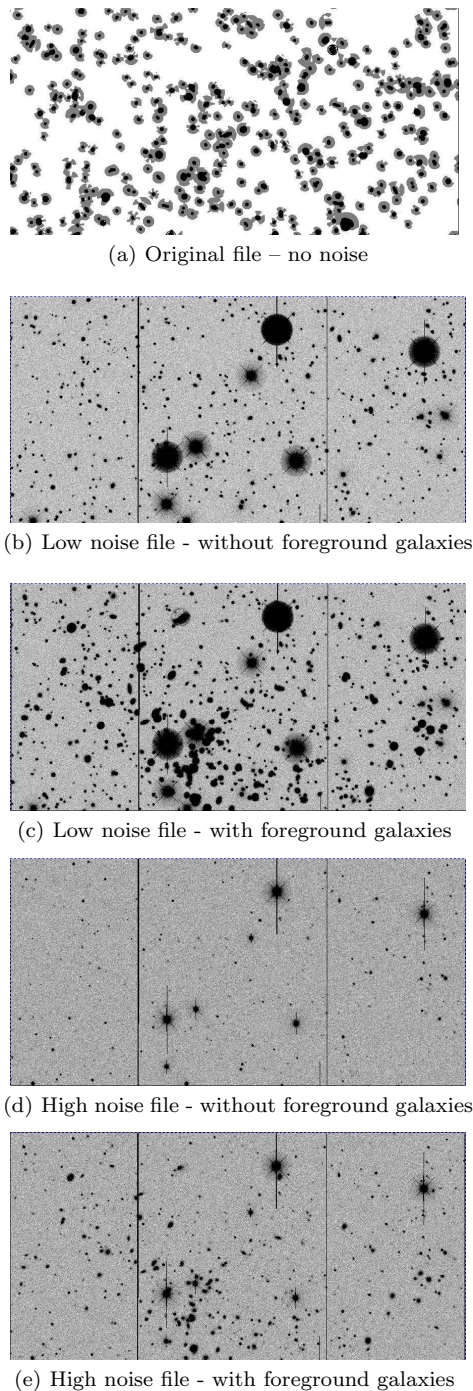


Figure 2. Partial focal plane images from the simulated cluster, for the portion containing the cluster, with size about 1000 pixels high, and 2000 pixels across. Background galaxies are visible as well as clear diffraction spikes (from the DECam telescope assembly) on the saturated foreground stars in the four images that contain them, and foreground cluster galaxies in the two images that contain them. It is clear that many more objects are seen in the low noise files. The vertical lines running from top to bottom in all four images with noise are bad CCD columns.

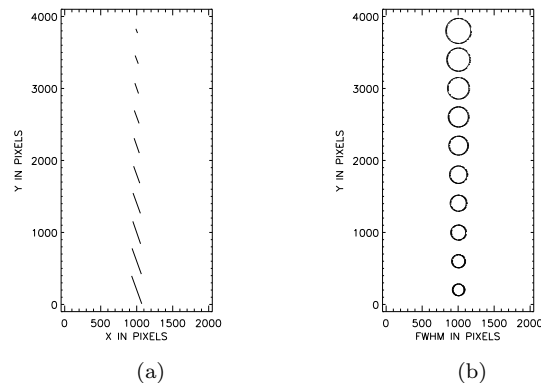


Figure 3. (a) Average of SExtractor ellipticities in horizontal strips in each CCD (the PSF pattern is identical for all CCDs), with the inclination of the segment indicating the direction of the average, and the length indicating its magnitude. (b) Average of the FWHM in cells in the same strips, with the radius of the circle indicating the scaled FWHM magnitude; specifically, with values chosen to make the variation visible: $\frac{(FWHM) - 2.8}{3.2} \times 1000$ (See Sec. 2.3).

nal from the true shear on the galaxy images, be corrected for properly by the PSF-removal algorithm.

3 PROCESSING THROUGH THE PIPELINES

3.1 Overview

In order to process a set of either simulated or real images and extract either a final cluster mass measurement or the SIS velocity dispersion σ_v , there are five fairly distinct steps that must be executed:

- (i) Find objects in the image and build a catalog of their properties.
- (ii) Use these properties to determine which of the objects are stars and which are galaxies.
- (iii) Use the objects determined to be stars to measure the PSF and remove its effect on the lensed galaxies.
- (iv) Refine galaxy selection with cuts that attempt to pick only galaxies behind the cluster.
- (v) Use the shear measurements to reconstruct a shear profile of the cluster and infer its mass or velocity dispersion.

We detail these steps in the following sections.

3.2 Source Extraction

As the first step in both the IMCAT and Shapelets pipeline, we execute Step (i) of Sec. 3.1 and extract objects from the image files using Source Extractor (or “SExtractor”, Bertin & Arnouts 1996). SExtractor runs over an image and builds a catalog of objects that contains various properties. Though the two pipelines invoke SExtractor in different ways, we use identical parameters in their respective configuration files and thus obtain fully identical SExtractor object catalogs from them with respect to the number of objects yielded and their properties. Our SExtractor configuration files are available on the website.

Right at the SExtractor level, we mask out neighbors (for both pipelines) by choosing only objects that survive the cut on the “overlap” flag, which indicates that SExtractor has found two objects within a predefined distance.

3.3 Star Selection

We next move to Step (ii) of Sec. 3.1, separating star and galaxy objects in the SExtractor object catalogs. Even though the star objects are very clear in this simulated cluster, it is useful to verify our star selection tools, which are needed for real images.

It is very important to have a good selection of stars when classifying objects because this determines the shape of the PSF that is later removed. Thus, we developed a number of tests to find the best sample of stars for our PSF determination. Our initial simulation here does not test our selection criteria very stringently, but we at least show for now how our tools work on this well-separated sample.

In general, stars are selected from an image by plotting the magnitude of the object vs. a measure of size such as the FWHM, and then selecting out the stellar locus in this figure, which is defined by objects that are small and fall in a very narrow range of sizes but a wide range of magnitudes. The FWHM is a standard output from SExtractor obtained by fitting the object with a Gaussian profile (see Sec. 8.4.4 of Holwerda 2005). The magnitude measure we chose to use from SExtractor, the MAG_AUTO output, is obtained by fitting the object to an elliptical aperture using second-order moments of its brightness (see Sec. 7.4 of Holwerda 2005).

In Fig. 4, we plot the magnitude vs. FWHM of objects in the LN image with noise, PSF, and foreground objects. In blue are objects that are known from the truth catalog to be stars, and in red are the “truth-matched” galaxies. We see clearly there the stellar locus, or “star column”, indicated by the objects contained in the vertical box on the left. Specifically, to isolate the “good star” objects we chose a FWHM of 2.9 to 3.3 pixels and a magnitude from 20.3 to 26. In the same figure we see several regions of stars, starting from the top arm stretching to the right: these are saturated stars which are not useful for PSF estimation. Moving down, we see in the vertical box in dark blue the good stars that are selected for the PSF shape estimation, and then in the region below this rectangular box stars that are dim and have poorly measured shapes, which we discard.

To make the initial selection of the galaxies, we use the information that they are generally larger than the stars in the number of pixels they cover, and have less surface brightness per pixel. They are thus generally characterized by larger FWHMs and fainter apparent magnitudes and they are the red objects on the right in Fig. 4. The magnitude limit we have chosen is approximately 26.5, though realistic r -band limits in DES will be closer to 24. The dimmer galaxies are in our sample primarily because the initial catalog we are working with has an i -band magnitude limit of approximately 24, but an attempt was made to make realistic color distributions, which resulted in fainter magnitudes in the r -band (see Sec. 2.1). We also note in the figure that there is a fairly sharp edge for the smallest galaxies. This is caused by a discrete lower cutoff in the size of the galaxies that were included in the simulation.

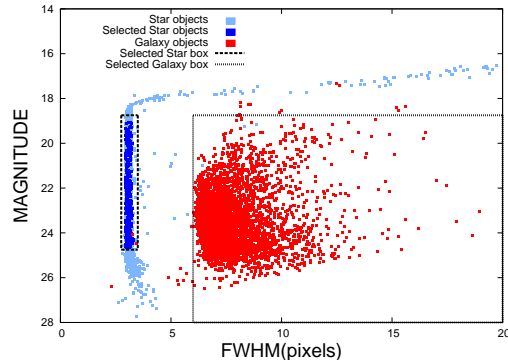


Figure 4. Magnitude (r -band) vs. FWHM (in pixels) for the LN image with noise, PSF, and foreground objects. Colors indicate the star and galaxy objects – stars in blue, and galaxies in red. Only 10% of the objects are shown for clarity. Note the separation between galaxies and stars is artificially large in this simulation, but in our future simulated images will be more realistic.

3.4 Galaxy Shape Estimators and PSF Removal

Moving next to Step (iii) of Sec. 3.1, we briefly describe the estimators the two pipelines use for the shapes of the galaxies, and the mechanisms by which they remove the PSF from the image, beginning with some formalism that is common to both pipelines.

3.4.1 Shapelets PSF Removal

To execute the Shapelets PSF removal pipeline, after selecting out the star objects, we form an initial shapelet model for each of them. We chose the maximum order of the initial stellar object decomposition to be $n_{max} = 20$. This is a hard limit that Shapelets is instructed to not go above in its creation of the decomposed object (Berge et al. 2006, Sec. 2.4). However, Shapelets uses a two-dimensional χ^2 -minimization algorithm (AMOEBa) to optimize both the order and size (beta) it chooses for the decomposition of each object by obtaining the best match between the reconstructed and original images – i.e. minimizing the residual (Berge et al. 2006, Sec. 2.3). For the stars, Shapelets converges on order $n = 12$ or 13 for each chip, and the average size of the stars is $\beta = 2.56 \pm 0.09$. At this point, all the stars are re-decomposed with the same order and size, to simplify the Shapelets PSF-removal algorithm (Berge et al. 2006, Sec. 3).

After all of the stars have been decomposed down to a shapelet model with a fixed order and width, we determine the order of the fitting function to interpolate each of the shapelet coefficients across the image plane and construct the PSF model. As the variation of our PSF was given by a simple linear function, we used a first order polynomial interpolation of the PSF.

The next step is to remove the PSF effects from the galaxy object Shapelets models. To do this, first we construct the galaxy using $n_{max} = 15$, since this was the order that the galaxies were made with. Shapelets again uses its minimization algorithm to find the optimal order and size for each object, and for most galaxy objects in our image, it chose $n = 10$ or 14 . The size β varies between about 2 and

Table 3. Average stellar ellipticities and their widths before and after PSF-removal stars on stars test (see Sec. 3.5).

File	$\langle e_1 \rangle$	$\langle e_2 \rangle$	σ_{e_1}	σ_{e_2}
Before PSF removal	-0.0132	-0.0110	0.0121	0.0112
After PSF removal	0.0008	0.0009	0.0095	0.0082

10, with an average of 4.6 and a standard deviation of 1.3. Now the interpolated PSF model constructed above is used at the position of each galaxy to removed the PSF effects on the galaxy.

Finally, in Shapelets it is possible to estimate the final shape of a galaxy in a number of ways, in this paper we use the minimal estimator, which is a ratio formed from three of the low order shapelet coefficients, specifically

$$\gamma_{\text{sh}} \equiv \frac{\sqrt{2}f_{22}}{f_{00} - f_{40}}, \quad (1)$$

(see e.g. eq. (39) of Massey et al. 2007b).

3.4.2 IMCAT PSF Removal

IMCAT also uses stars to remove the PSF-induced alteration of the size and ellipticity on the galaxy objects, relying on just quadrupole moment shape measurement rather than the entire decomposition of the shape into basis functions of an orthogonal set. It relies on the KSB algorithm (Kaiser et al. 1995) which is well-tested and whose variants continue to be widely used in cluster weak lensing analyses (for just a few examples, see Mahdavi et al. 2007, Gavazzi et al. 2009, Holhjem et al. 2009, Miyazaki et al. 2007, Umetsu et al. 2007) as well as for cosmological shear, e.g. Hettterscheidt et al. (2006). It has been found that the matrices which correct for the anisotropic and isotropic piece (the “smear” and “shear” matrices) are nearly diagonal in practice (Luppino & Kaiser 1998, Hoekstra et al. 2008, and Sec. 4 of Bacon et al. 2001), and this is the KSB implementation we use.

3.5 PSF Removal Test

In order to test how well we are removing the PSF, we implemented a test that we refer to as a ‘stars on stars’ test. Here we randomly selected half of the stars to calculate the PSF distortion and apply this correction to the other half of the stars. In general, the size of the corrected stars in such a test should become smaller and the ellipticities of these stars should shrink substantially.

Because a linear variation in ellipticity and size of the stars was put into the PSF, we expect that a linear order interpolation of the PSF will be sufficient to adequately describe the PSF across each CCD. This is indeed what we find; numerically, after a linear order PSF correction, taking the 200–300 stars per CCD on the files and dividing them into two groups, we find the values in Table 3 for the average and width of the values of the ellipticities of the PSF-corrected stars. These results indicate a reduction by between one and two orders of magnitude in the average of each component of the ellipticity, and a reduction by about a third in the ellipticity width distribution.

We also did this at several other orders of the PSF functional interpolation polynomial. As one would expect, at zeroth order (constant stellar ellipticity and size assumed across whole plane), we found that in fact the average ellipticities were of the same order as before correction, and the widths barely shifted. Above order one, there was no significant reduction in either the average ellipticities nor widths above that already gained by the order one PSF removal. This confirms that a first order interpolation is sufficient to describe the PSF variation across the CCD. Of course, higher order interpolation is in general needed for real images, which will not have such a simple PSF structure or variation with spatial position.

4 RESULTS

Having discussed our methods and tests, we now move to the results from running both pipelines on the simulations.

4.1 Fitting SIS Profiles

For an SIS cluster, the critical Einstein radius for each background galaxy is

$$\theta_E = \left(\frac{4\pi\sigma_v^2}{c^2} \right) \frac{D_{ls}(z_l, z_s)}{D_s(z_s)}, \quad (2)$$

where σ_v is the intrinsic three-dimensional lensing cluster galaxy velocity dispersion, $D_{ls}(z_l, z_s)$ is the angular diameter distance from the lens to this background source galaxy, and $D_s(z_s)$ is the distance from the observer to the background galaxy (see e.g. Sec. 3.1.5 of Bartelmann & Schneider 2001, Schneider et al. 2005, Munshi et al. 2006).

Also for a SIS model the shear from a cluster on a given background galaxy depends on the Einstein radius simply as

$$\gamma(\theta) = \frac{\theta_E}{2\theta}. \quad (3)$$

where θ is the projected radial distance of a background galaxy from the center of the cluster. Eq. 3 is the shear of any observed galaxy, and because of the distance ratio $D_{ls}(z_l, z_s)/D_s(z_s)$ in the Einstein angle, a galaxy at the same radial distance from the center of the cluster but at a different background redshift is sheared differently. However, if the exact redshift for a specific lensed galaxy and thus its distance ratio factor is known, we may divide through by this and remove this variation. In this manner, we obtain a set of points for the shear as a function of projected radial distance of a background galaxy from the center of the cluster. We may then fit a hyperbolic function to this set of points and invert the above equations to obtain a value for σ_v .

In the case where neither the spectroscopic nor photometric redshift of a galaxy is available, we may obtain a value for the distance ratio assuming each galaxy lies at the average of the redshifts of all the background galaxies, i.e. use the “single sheet approximation”, an approach still often taken in weak lensing work (e.g. McInnes et al. 2009, Holhjem et al. 2009, Gavazzi et al. 2009, Mahdavi et al. 2007).

4.1.1 Fitting PSF-removed Files

We now move to the core of the lensing pipelines, the extracted σ_v results after we have processed the files through each pipeline and removed the effect of the PSF.

We did tests correcting galaxies for the extracted PSF in three different ways: (1) by extracting the PSF from a fit to the stars in each CCD separately, as would typically be done with real data; (2) by grouping stars from all CCDs with their relative position on that CCD into one “super” CCD and extracting the PSF from a fit to the stars in the super-CCD; (3) by extracting the PSF from a fit to 10 ‘truth stars’. These ‘truth stars’ are extracted from an image we constructed with one star in each of the 10 discrete y-positions on the CCD, each affected by the PSF for that specific y-position.

We found that the profile results changed very little whichever way we extracted the PSF, which is reasonable in this simulation because the PSF is replicated for each CCD, and because we found that the SExtractor stellar properties are such a close match to the truth star ones. Thus, we chose to remove the PSF in the way closest to how it would be done in the real world, namely by extracting the PSF from a fit to the stars in each CCD. In future simulated images, we will more realistically vary the PSF across the entire focal plane. This is the plan for Data Challenge 5 for DES, scheduled to begin in Autumn 2009.

Though we will show results from all the files with a PSF, we choose the Low Noise file with foreground galaxies as our primary reference file, because it has several of the major realistic features – i.e. a PSF, foreground stars and galaxies – and can be processed through both of our pipelines. However, it does have low noise relative to the expected DES exposures (see Sec. 2.2), and this is to be kept in mind when reviewing results. We will examine the scaling of the error in the output σ_v from the corresponding high noise version in Sec. 5.1.3.

After removing the PSF, we make a cut of $|(\gamma_1, \gamma_2)| < 2$ on each of the resulting two components of shear for each galaxy as is regularly done in lensing pipelines⁴. Further, though we made the initial galaxy cut to remove stars, we next refine our selection by making a color cut of $r - i > 0.7$ (see Sec. 5.1.1) to remove all the foreground galaxies. We then average the galaxy ellipticities in radial annular bins to determine the shear at that radius, and fit the results according to Sec. 4.1. Again we use a simplification of using the known center of the cluster to determine the annular bins, focussing for now on the issue of shape measurement of the galaxies. In Table 4 we show the results of this analysis on this file, compared to doing the same fit on only the averages of the SExtractor ellipticities of the objects in the same bins, and we see that though the error bars are larger by a factor of 2-3 from the SExtractor case, more significantly, the central value from each pipeline is now within one sigma of the input, where it was over 11 σ away before. The error bars become larger essentially because, as part of the PSF-

⁴ Technically, this is because removing the PSF requires a step of division by the polarizability. However, the polarizability can approach zero for objects whose shape is badly determined, leading to the shear mathematically increasing to very large and unphysical values.

removal process in each pipeline, the step of dividing by an often small polarizability increases the intrinsic shape error of each galaxy. This behavior is regularly seen in all lensing pipelines.

The results in Table 4 are shown for 49k objects that have been position-matched between the final IMCAT and Shapelets catalogs (and the truth catalog, to make the color cut to keep background galaxies). Another way to do this comparison is by only matching each of the catalogs to the truth catalog so that the color cut to keep background galaxies can be made, but not matching the objects in each pipeline with one another, and the results for these fits are shown in the last two lines of the same table.

In Fig. 5 we show the E- and B-mode binned profiles corresponding to the results in Table 4 and compared again to the input shear. It is clearly seen that in the innermost bins, the Shapelets shear is above the input, and the IMCAT shear lies below the input, which is what leads to the σ_v values of Table 4. The B-mode points are generally consistent with zero across the plane and we checked that these are well-fit to a nearly flat line in all cases.

5 VARIATIONAL STUDIES

Having a simulated cluster in hand for which we know all the properties, we are able to do controlled studies from which we learn how the extracted σ_v varies with varying several types of cuts and weightings. Though we are working with idealized quantities in several properties of the galaxies such as their colors, we reiterate that our primary goal was to check whether the two pipelines work in the high shear regime, and we do these studies only to indicate what we might expect from varying some of the cuts we make on our accepted galaxies. In our later studies, we will follow up with more realistic color distributions and photometry.

5.1 Galaxy Cut Variation Studies

5.1.1 Color Cuts

At times, one must remove the foreground and cluster galaxies when one has no spectroscopic nor photometric redshift information on the galaxies, such as when one has only 2 or 3 photometric bands for each object, and cannot effectively make photometric redshift estimates. In these circumstances, to most effectively remove foreground objects from the sample, one most often one resorts to making a color cut on objects, as foreground and background galaxies are located in different loci of color space. By examining the distribution of the simulated objects, for which precise redshifts and magnitudes in various idealized colors are known, it is possible to determine a color cut which will remove most of the foreground galaxies.

Though in reality of course it is more difficult to make the correct color cuts as we do not have perfect photometry in the various bands, our goal here in this section is to simply suggest how much difference cuts with differing levels of purity would affect the determination of the cluster properties.

In For the reference file, we chose the simple $r - i > 0.7$ cut shown in Fig. 6 (Cut A), and we describe in the

Table 4. Values of σ_v derived from the binned fits to the shear after the PSF has been removed, compared to the fit to the SExtractor-only ellipticities, with all objects from the same position-matched file (this corresponds to Fig. 5). The “ σ Deviation” is the number of σ that the result is away from the input value of $\sigma_v = 1250$ km/sec, i.e. $\sigma = (\text{result} - \text{input})/\sigma_v$. For the χ^2/dof the number of degrees of freedom is 11 because we restrict the fit range to less than the total extent of the image plane (see text). The central value from the shear output from each pipeline is within one sigma of the input, while it is over 11σ away before PSF-removal.

File	Redshift	σ_v (km/s)	σ_{σ_v} (km/s)	χ^2/dof	σ Deviation
SExtractor Value LN PSF Applied File	0.84	954	26	12.9/12	11.4
Matched IMCAT Value LN PSF Removed File	0.84	1215	74	13.1/11	-0.5
Matched Shapelets Value LN PSF Removed File	0.84	1291	108	13.5/11	0.4
Non-matched IMCAT Value LN PSF Removed File	0.82	1224	59	10.2/11	-0.4
Non-matched Shapelets Value LN PSF Removed File	0.80	1373	102	20.2/11	1.2

same figure three other ways one might make this color cut. We also show in the same figure which galaxies would be excluded given these color cuts on a well-calibrated CFHT control sample, which is described in Ilbert et al. (2006) as Field “D1”. In Fig. 7, we show the effect varying the color cut has on the determination of σ_v . We see from this figure that the various possible ways of making color cuts have no dramatic effect on the σ_v values, except for Color Cut D for which the fit values for the truth and IMCAT deviate the most from the others. We note here also that the Shapelets results are consistently larger and both IMCAT and Shapelets generally track the truth value.

5.1.2 Size Cuts

Though we began as we saw with a unrealistically large size segregation between stars and galaxies, we may still investigate what effect cutting into the size distribution of the galaxies we have has on the extracted cluster properties. To this end, various cuts on size are used to attempt to eliminate the error due to poor ellipticity and shear estimation. A larger object should in general have less error in its ellipticity and shear estimation, as they are less affected by the noise in the pixels immediately surrounding the galaxy (the fainter the galaxy, the more this effect is seen). The effect on the extracted σ_v from various cuts on the galaxy FWHM are shown in Fig. 8. We see mild variation in σ_v as a function of FWHM cut, with both the Shapelets and IMCAT σ_v tending slowly toward the input as smaller objects are cut out. This indicates that the better measurement of the shape of larger objects yields somewhat better final results. However, there is a tradeoff in that the error bars are also seen to grow steadily as the statistics are reduced (by about 49k to 37k galaxies from the mildest to strictest cut, a factor of about 25% fewer objects). Since magnification is not included in our simulation, we of course cannot quantify from these images yet further effects on the shear profile such as the effect of faint and small background galaxies becoming larger and magnified enough to be seen behind the cluster, also referred to as “lensing bias” (Schmidt et al. 2009a, Schmidt et al. 2009b).

5.1.3 Noise Variation

Shapelets was not able to work on the High Noise files⁵, so the results in Fig. 9 are for IMCAT only. The Low Noise values have smaller error bars than the High Noise values, and this is only partly accounted for by the smaller number of objects in the HN images. In fact, the LN file has about 49k objects, and the HN one 23k, and the extracted σ_v for LN is 1215 ± 74 km/sec where that for HN is 1227 ± 135 km/sec. However, if we scaled the error bars just by statistics from LN to HN, we would obtain 108 km/sec. Thus, the HN error is a factor of about 25% higher than just statistical scaling, indicating that the higher noise has led to a wider spread in the shear estimates of the objects.

From this we see that higher noise is harmful to profile extraction not only for suppressing statistics, but intrinsically in worsening shape estimation of objects.

6 CONCLUSION

As a first step in a longer term campaign of studying cluster weak lensing in simulations in detail, We have run two independent weak lensing analysis pipelines on a suite of simulated galaxy cluster images created in the framework of the simulation tools developed by the Dark Energy Survey. This simulation contains noise, foreground objects, and a PSF which varies both in FWHM and ellipticity. Both pipelines give results that are within the one-sigma error bars of the input value using the same processing that would be applied to real data. Thus, our analysis of this DES cluster simulation demonstrates that both the IMCAT and Shapelets pipelines are able to reproduce the input singular isothermal sphere σ_v in at least this simulation with a few more realistic features than have been implemented in previous weak lensing simulation efforts such as the STEP and GREAT challenges (Heymans et al. 2005, Massey et al. 2007a, Bridle

⁵ This is regularly seen, and occurs essentially because IMCAT needs only a few parameters to describe the shape of the ellipse that circumscribes an object, while Shapelets aims to extract the total shape information of an object into a coefficient basis, and will fail to actually obtain a Shapelets decomposition for an object more often in low S/N situations where the edges are less well-defined.

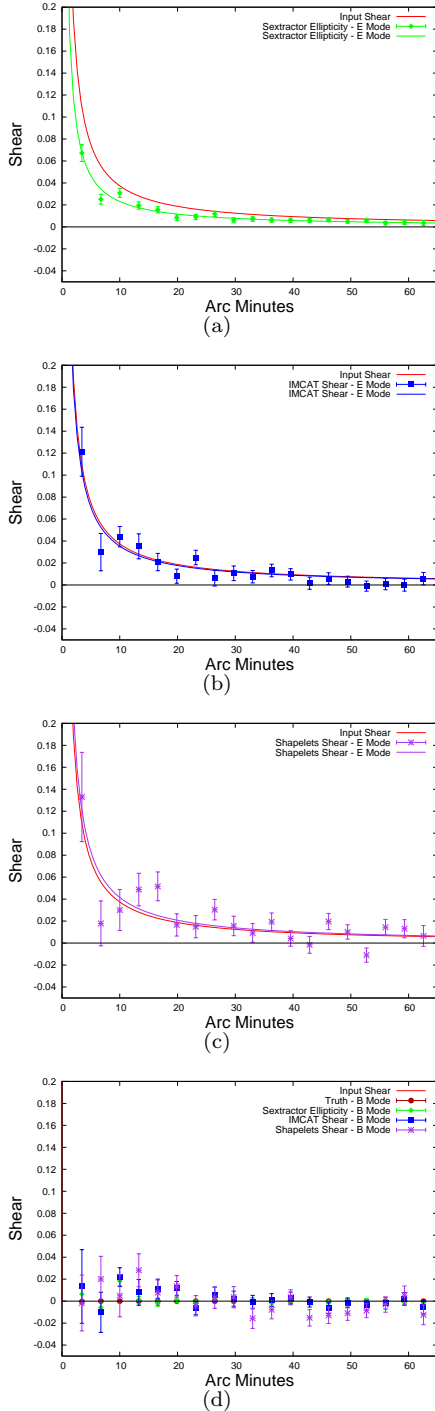


Figure 5. Profiles for SExtractor and PSF-removed files compared to the input for the entire image plane from the reference file (see Sec. 4.1.1) – i.e. the Low Noise file with foreground galaxies removed by color cut, all galaxies redshift-corrected to $z = 0.84$ (see Sec. 5.1.1), and all objects position-matched between the IMCAT and Shapelets files. This results in a single file of 49.2k objects. The fit profiles correspond to the values in Table 4. The red solid line corresponds to the input value in all cases, and also shown are the binned data points and the fit profile to the unbinned points. Shown are the values for (a) SExtractor ellipticities (b) PSF-removed IMCAT shear and (c) PSF-removed Shapelets shear.

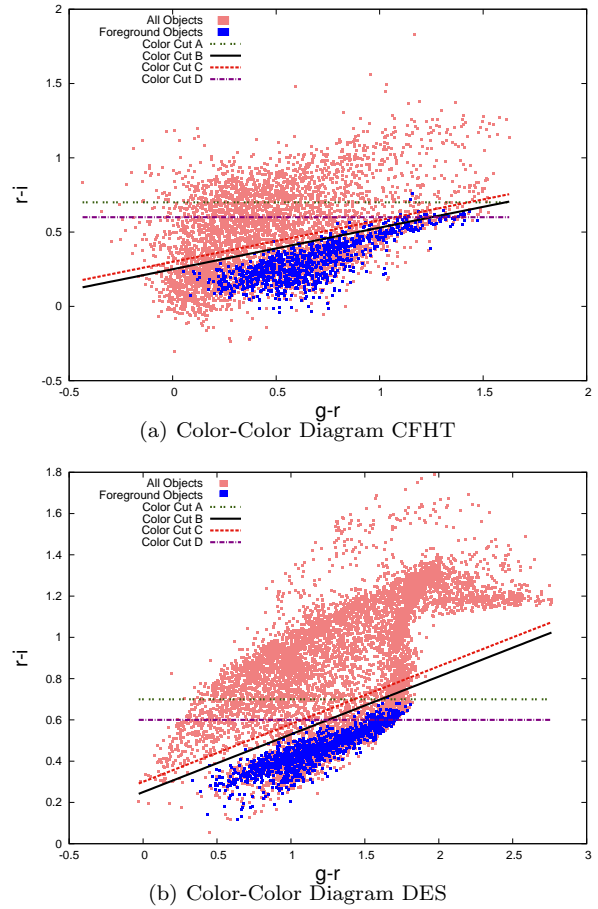


Figure 6. Color-Color Plots for the Low Noise file with foreground galaxies. For CFHT, color and photometric redshift information is from observations, while for our simulated image, the color and redshift information is obtained from a match to the truth files, for which such information is available (see Sec. 2.3). “Color Cut A” selects the objects for which $r - i$ is greater than 0.7. “Color Cut B” selects the objects for which $r - i$ is greater than $(g - r) \times 0.28 + 0.25$. “Color Cut C” selects the objects for which $r - i$ is greater than $(g - r) \times 0.28 + 0.3$. “Color Cut D” selects the objects for which $r - i$ is greater than 0.6. Note that though the Color-Color diagrams for CFHT and DES look fairly different, the same color cuts do seem to have similar effects in how much foreground contamination is removed for both of them.

et al. 2010), such as a PSF that varies in size and ellipticity across the focal plane.

With this simulation it was possible to also test more realistic galaxy selection cuts such as those made on color and size, as well as vary the fit limits and star selection, and demonstrate that the pipelines were able to handle these different choices robustly. It seems as though IMCAT can handle images with a high level of noise more robustly than Shapelets, although both pipelines performed better on images with a low level of noise. Low noise images are of course the type of images that large aperture telescopes with long exposure times, so our results indicates either pipeline would work well for such images. And while this work indicates that Shapelets may not be optimal for future rapid cadence surveys where images may not be stacked until after several

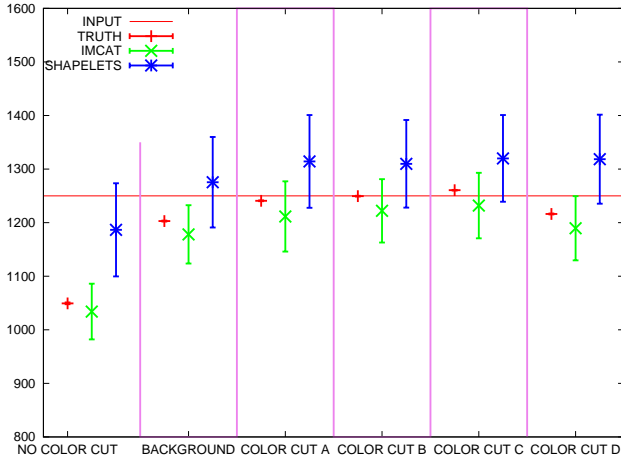


Figure 7. Variation of σ_v with varying color cuts. The red crosses represent the effect of doing the cut on the truth values of the shear for each object, the green x's the same on the IMCAT values of the shear for each object, and the red *'s the same on the Shapelets. Cut labelling is as in Fig. 6. All objects are corrected to the single sheet approximation value of $\langle z_b \rangle = 0.84$. In the column labelled “Background” we have used the truth information on the redshift of each object to select all the true background galaxies.

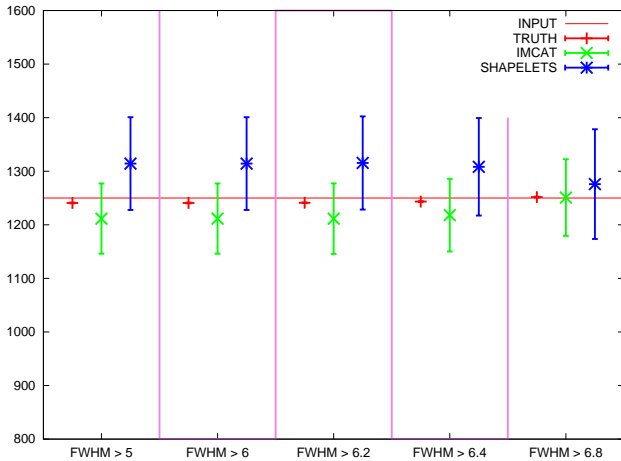


Figure 8. Variation of σ_v for various FWHM Cuts. Symbols are as in Fig. 7. All objects are corrected to the single sheet approximation value of $\langle z_b \rangle = 0.84$. The cuts range from “no cut” in the leftmost panel (i.e. $\text{FWHM} > 5.0$ pixels, as is already done for the initial galaxy selection) to $\text{FWHM} > 6.0, 6.2, 6.4, 6.8$ pixels in the following four panels.

years, we do point out we have only worked thus far with our implementation and configuration of the method and code.

Using both of these independent pipelines and potentially others in parallel on the same future cluster data samples will provide an internal crosscheck which will give confidence on shear estimates and masses extracted from cluster weak lensing analyses. We find that dominant errors are from noise and galaxy statistics, thus it is important to have a large enough galaxy sample in an image with as low as possible noise properties in order to get the optimal shear pro-

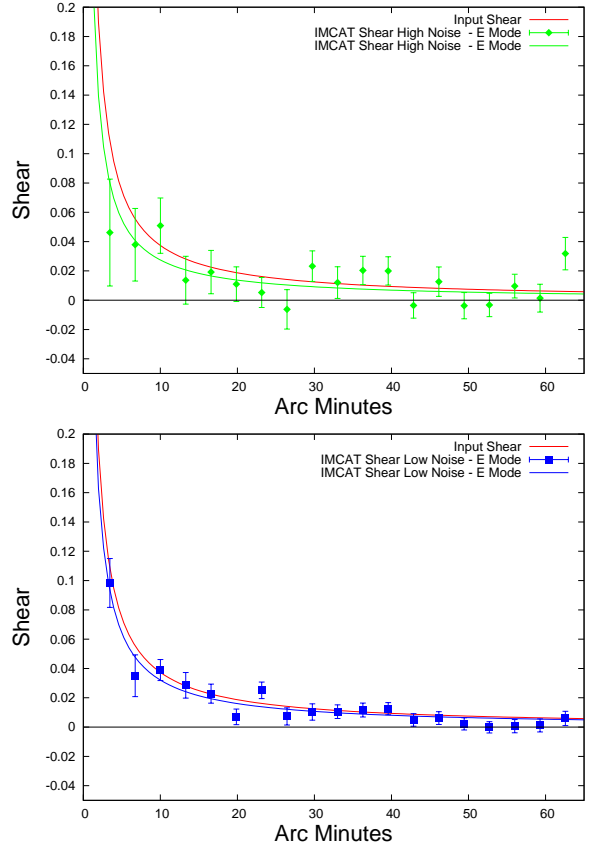


Figure 9. Fit profiles and binned points for two levels of noise. All objects for the (a) High Noise file are corrected to the single sheet approximation value of $\langle z_b \rangle = 0.64$ (23.1k objects), All objects for the (b) Low Noise file are corrected to the value of $\langle z_b \rangle = 0.84$ (49k objects). The χ^2_{dof} is 13.2/12 for the LN file, and 8.2/12 for the HN one. Note the larger error bars on the HN points (see text in Sec. 5.1.3).

file. We will follow this study with future analyses on suites of multiple weakly lensed cluster images with differing noise levels with different shear profiles (such as an NFW profile) to do statistical tests on the pipelines.

We have made the suite of images used in this analysis publically available for others to analyze at <http://ccapp.osu.edu/DEScluster>.

ACKNOWLEDGMENTS

The simulated images used in this study are based on the DES mock galaxy catalog created by M. Busha and R. Wechsler, and we fully express our appreciation to them for being able to use these catalogs.

We would like further to very much thank D. Applegate, J. Beacom, J. Berge, G. Bernstein, S. Bridle, J. Cohn, D. Clowe, G. Evrard, J. Frieman, S. Habib, B. Jain, M. Jarvis, C. Kochanek, K. Kuehn, S. Kazantzidis, A. Leauthaud, R.J. Massey, T. McKay, R. Nakajima, C. Orban, B. Ragazzone, B. Rowe, E. Sheldon, A. Slosar, G. Steigman, M. White, H. Yan, and A. Zentner for many helpful discussions, pointers and readings.

REFERENCES

- Abbott, T. et al., The Dark Energy Survey Collaboration, modified version of White Paper submitted to the Dark Energy Task Force [arXiv:astro-ph/0510346]
- Albrecht et al., Dark Energy Task Force Report, 2006 [arXiv:astro-ph/0609591]
- Bacon, D., Refregier, A., Clowe, D., Ellis, R. *Mon.Not.Roy.Astron.Soc* Volume 325, Issue 3, Pages 1065-1074 [arXiv:astro-ph/0007023]
- Bartelmann, Matthias and Schneider, Peter, 2001, *Phys. Rept.*, [arXiv:astro-ph/9912508]
- Berge, J., Massey, R., Refregier, A. – unpublished, but available at this [URL](#)⁶
- Bernstein, G.M. and Jarvis, M., 2002, [arXiv:astro-ph/0107431]
- Bertin, E., Arnouts, S., 1996, *Astronomy and Astrophysics Supplement*, 117,393
- Blanton, M. R., et al. 2003, *ApJ*, 592, 819
- Bridle, S., et al. *Annals of Applied Statistics* 2009, Vol. 3, No. 1, 6-37 [arXiv:0802.1214]
- Bridle, S., et al. Accepted in *MNRAS*, 2010 [arXiv:astro-ph/0908.0945]
- Colberg, J. M., et al. 2000, *MNRAS*, 319, 209 [arXiv:astro-ph/0005259]
- Gavazzi, R. et al. *Astronomy and Astrophysics*, Volume 498, Issue 2, 2009, pp.L33-L36 [arXiv:astro-ph/0904.0220]
- Gerdes, D.W., et al. 2009, submitted to *Astrophys.J.* [arXiv:0908.4085]
- Hettterscheidt et al. *Astronomy and Astrophysics*, Volume 468, Issue 3, June IV 2007, pp.859-876 [arXiv:astro-ph/0606571v1]
- Heymans, C., et al. 2005, *MNRAS* 368 1323 (STEP1) [arXiv:astro-ph/0506112]
- Hoekstra, H., Franx, M., Kuijken, K., and Squires, G. (1998). Weak Lensing Analysis of CL 1358+62 Using Hubble Space Telescope Observations <http://adsabs.harvard.edu/abs/1998ApJ...504..636H>. *ApJ* 504, 636. [arXiv:astro-ph/08103600v1]
- Holhjem, K., Schirmer, M., Dahle, H. *Astronomy and Astrophysics*, Volume 504, Issue 1, 2009, pp.1-13 [arXiv:astro-ph/0906.2938]
- B.Holwerda, 2005, [arXiv:astro-ph/0512139v1]
- K. Honscheid, et al. 2008, [arXiv:astro-ph/08103600v1]
- Ilbert, O. et al. *Astronomy and Astrophysics*, Volume 458, Issue 1, October IV 2006, pp.39-52 [arXiv:astro-ph/0603202]
- Kaiser, N., Squires, G., & Broadhurst, T. 1995, *ApJ*, 449, 460
- Luppino, G. and Kaiser, N. *Astrophys.J.* 475 (1997) 20 [arXiv:astro-ph//9601194v1]
- Monet, D., et al. 2003, *AJ*, 125, 948
- Mahdavi, A., et al. *The Astrophysical Journal*, 2007, Volume 664, Issue 1, pp. 162-180. [arXiv:astro-ph/0703372v1]
- Massey, R. et al. 2007, *MNRAS* 376 13 (STEP2) [arXiv:astro-ph/0608643v2]
- Massey, R. et al. 2007, *MNRAS* 380, Issue 1, pp. 229-245 [arXiv:astro-ph/0609795]
- McInnes, R. et al. *Monthly Notices of the Royal Astronomical Society: Letters*, Volume 399, Issue 1, pp. L84-L88. [arXiv:astro-ph/0903.4410]
- Miyazaki et al. *The Astrophysical Journal*, Volume 669, Issue 2, pp. 714-728. [arXiv:astro-ph/0707.2249]
- Munshi et al. *Physics Reports*, Volume 462, Issue 3, p. 67-121. [arXiv:astro-ph/0612667]
- Narayan, R. and Bartelmann, M. , 1996 , [arXiv:astro-ph/9606001v2]
- Peng, C.Y. et al. *AJ*, 124, p. 266 (2002) [arXiv:astro-ph/0204182]
- Peacock, J.A., Schneider, P., Efstathiou, G., Ellis, J.R., Leibundgut, B., Lilly, S.J., Mellier, Y.; ESA-ESO Working Group on “Fundamental Cosmology” . *Tech. Rep. Oct.* [arXiv:astro-ph/0610906]
- Refregier A. 2003, *MNRAS* 338 35 [arXiv:astro-ph/0105178v1]
- Scoville, N., et al. 2007, *ApJS*, 172, 1
- Schmidt, F., Rozo, E., Dodelson, S., Hui, L., Sheldon, E., *Phys. Rev. Let.* 103, 051301 (July 2009) [arXiv:0904.4702]
- Schmidt, F., Rozo, E., Dodelson, S., Hui, L., Sheldon, E. , *Journal-ref: Astrophys.J.702:593-602,2009* [arXiv:0904.4703]
- Schneider, P. et al. *Gravitational Lensing: Strong, Weak and Micro, Saas-Fee Advanced Courses*, Volume 33. ISBN 978-3-540-30309-1. Springer-Verlag Berlin Heidelberg, 2006, p. 269 [arXiv:astro-ph/0509252]
- Umetsu, K., Takada, M., Broadhurst, T., *Modern Physics Letters A*, Volume 22, Issue 25-28, pp. 2099-2106 (2007) [arXiv:astro-ph/0702096]
- Wechsler, R et al. in preparation.
- Wechsler, R, “Interpreting SDSS Cluster Masses and Abundances with Mock Catalogs” in *Clusters of Galaxies: Probes of Cosmological Structure and Galaxy Evolution*, from the Carnegie Observatories Centennial Symposium. Carnegie Observatories Astrophysics Series. Edited by J.S. Mulchaey, A. Dressler, and A. Oemler, 2004. Pasadena: Carnegie Observatories.

⁶ <http://www.astro.caltech.edu/~jberge/Publicationsfiles/shapeletsmanualv2t1.pdf>